Optical Techniques for Advanced Salt Systems

Prepared for
US Department of Energy

Shirmir D. Branch, Heather M. Felmy, Jason M. Rakos, Suhee Choi, Forrest D. Heller, Bruce K. McNamara, Sergey I. Sinkov, Samuel A. Bryan, Amanda M. Lines

Pacific Northwest National Laboratory

September 2025
PNNL-38262

DISCLAIMER

PACIFIC NORTHWEST NATIONAL LABORATORY
operated by
BATTELLE
for the
UNITED STATES DEPARTMENT OF ENERGY
under Contract DE-AC05-76RL01830

Printed in the United States of America

Available to DOE and DOE contractors from
the Office of Scientific and Technical Information,
P.O. Box 62, Oak Ridge, TN 37831-0062
www.osti.gov
ph: (865) 576-8401
fox: (865) 576-5728
email: reports@osti.gov

Available to the public from the National Technical Information Service
5301 Shawnee Rd., Alexandria, VA 22312
ph: (800) 553-NTIS (6847)
or (703) 605-6000
email: info@ntis.gov

Online ordering: http://www.ntis.gov

Optical Techniques for Advanced Salt Systems

September 2025

Shirmir D. Branch
Heather M. Felmy
Jason M. Rakos
Suhee Choi
Forrest D. Heller
Bruce K. McNamara
Sergey I. Sinkov
Samuel A. Bryan
Amanda M. Lines

Prepared for
the U.S. Department of Energy
under Contract DE AC05 76RL01830

Pacific Northwest National Laboratory
Richland, Washington 99354

SUMMARY

Molten salt reactors (MSRs) are receiving significant interest world-wide as a Gen IV nuclear reactor design that can safely and efficiently deliver reliable and resilient energy. However, the means by which material will be accounted for within these systems still needs to be determined. This report covers recent advancements in the exploration of optical spectroscopy for use in on-line monitoring of molten salts. On-line monitoring tools can provide *in situ* and real-time insight into process conditions. Utilizing optical tools such as UV-vis absorbance and Raman spectroscopy can provide highly detailed information on the chemical composition, not only by quantifying analytes such as uranium (U) or plutonium (Pu) but also in determining oxidation states and speciation. Connecting this information with more traditional radiometric information can offer an avenue to accurately quantify target analytes in a more robust way that can be broadly applicable to the variable and complex conditions expected at MSRs. To accomplish this, R&D is needed to both advance ultra-violet (UV-vis), near-infrared (NIR) and Raman approaches and to develop the data fusion approaches to connect the resulting data to radiometric data.

Work accomplished in FY25 took essential and successful steps to address these research and development (R&D) needs. This included a proof of principle demonstration of fusing UV-vis, Raman, and gamma data, which was covered in an earlier report.[1] The content of this report focuses on the advancement and demonstration of optical techniques to quantify key analytical targets within a molten salt. Examples include demonstrating Pu identification and quantification in the presence of interferences within a molten salt. Isolating temperature impacts on Pu fingerprints as well as expanding knowledge of Pu fingerprints in multiple oxidation states and in the NIR region. Advancing small scale systems for cost effective and efficient collection of optical libraries was also completed. Finally, an evaluation of uncertainty of analysis was explored, with results showing promise for future applications.

Recommended next steps include leveraging FY25 work to advance the data fusion approaches for optical and radiometric data sets. Ultimately, the combination of these data streams may offer the needed flexibility and robustness necessary to enable comprehensive on-line and real-time material control and accounting.

This report meets milestone M2RS-25PN0401041: Optical spectroscopy training set development of advanced analyte systems.

CONTENTS

FIGURES

TABLES

ACRONYMS AND ABBREVIATIONS

ARDP	Advanced Reactor Demonstration Program
ARSS	Advanced Reactor Safeguards and Security
DOE	US Department of Energy
FY	fiscal year
GAIN	Gateway for Accelerated Innovation in Nuclear
IP	intellectual property
LOD	limit of detection
LWR	light water reactor
MC&A	material control and accounting
MCR	multivariate curve resolution
MSR	molten salt reactor
NIR	near infrared
OLM	on-line monitoring
PLS	partial-least squares
PNNL	Pacific Northwest National Laboratory
RMSEC	root-mean-square error of calibration
RMSECV	root-mean-square error of cross validation
RMSEP	root-mean-square error of prediction
TRU	transuranic
UHP	ultra-high purity
UV-vis	ultra-violet visible

1. INTRODUCTION

Molten salt reactors (MSRs) are seen as promising advanced reactor technologies to efficiently meet growing energy demands. Numerous technological demonstrations are currently being conducted through DOE, industry, and national laboratory efforts. While these designs can offer various advantages in safety and efficiency, they do represent an area where more traditional material control and accounting (MC&A) approaches might not be applicable. One of the challenges with liquid fuel reactors is the movement of radioactive inventory throughout the primary reactor loop. This can be further complicated by designs that utilize on-line refueling, processing, recycling, and waste handling.

On-line monitoring (OLM) provides a key opportunity to aid in tracking and accounting inventory in these complex molten salt chemical systems. OLM has the potential to provide continuous insight into MSR material boundary areas (MBAs) when compared to traditional grab sample analysis for MC&A. Furthermore, OLM techniques can serve as a method to detect chemical changes in a system (e.g., precipitation) that may impact accurate MC&A. The challenge would be adapting these technologies for the application to the high temperature and highly corrosive environments of these MSR systems.

Ultimately, multiple sensor types will likely be needed to provide the comprehensive input needed for fully informed MC&A. One highly beneficial technology to include is optical spectroscopy, which can provide unparalleled insight into chemical speciation, redox states, and concentrations in molten salt systems.[2-9] These technologies can provide powerful tools for the accurate accounting of actinides and other analytes of interest within the complex chemical systems in molten salt environments. Furthermore, optical monitoring approaches can be combined with advanced analysis techniques such as chemometric modeling for the real-time and accurate analysis of optical data.[10-16] However, transitioning these technologies to molten salt systems requires key technology advances, which were identified and outlined in previous reports.[16-19] Furthermore, identifying routes to fuse data from disparate sensors is needed to improve robustness and flexibility of application of on-line monitoring.[1]

Project work in FY25 was focused on demonstrating the measurement uncertainty of a target transuranic (TRU) element [i.e., plutonium (Pu)] in the presence of interfering species. This included efforts such as synthesizing and purifying salt systems of interest, measuring spectra of pure component and mixed analyte systems using multiple optical analytical techniques, and combining that optical information to model and predict the concentration of the target species in the presence of mixed analyte systems. This also allowed for the determination of a measurement uncertainty for Pu using these techniques. In addition, advancements were made in understanding temperature impacts to Pu spectral fingerprints as well as expanding knowledge of spectral fingerprints in multiple oxidation states and across the visible (vis) and near infrared (NIR) optical ranges.

2. Chemical Materials and Preparation

2.1. Reagents and Materials

Lithium chloride (LiCl, Thermo Scientific, 99%) and potassium chloride (KCl, Thermo Scientific, 99.0-100.5%) were purified in-house as described in Section 2.3. Neodymium (III) chloride ($NdCl_3$, Thermo Scientific, 99.9%), dysprosium (III) chloride ($DyCl_3$, Thermo Scientific, 99.9%), zirconium chloride ($ZrCl_4$, Sigma Aldrich, 99.99%), potassium hydroxide (KOH, Fisher Scientific), LiCl-KCl eutectic (Sigma Aldrich, 99.99%), sodium nitrate ($NaNO_3$, Sigma Aldrich, ACS reagent, ≥99.0%), and hydrochloric acid (HCl, Sigma-Aldrich) were purchased from the manufacturer and used without further purification. Plutonium(III) and Pu(IV) chlorides were synthesized in-house as described in Section 2.4.

2.2. Inert Box Setup

All molten salt experiments were conducted in an inert glovebox. The atmosphere in the glovebox is maintained at <1 ppm O_2 and <5 ppm moisture. The box pressure is maintained at -1.1” w.c. The inert atmosphere was provided by ultra-high purity (UHP) argon. Sample holders were thoroughly cleaned and dried at >150 °C prior to being placed into the glovebox. The inert glovebox is approved for the handling of safety-significant materials as well as high-temperature systems such as molten salts.

2.3. Eutectic Salt Purification

The purity of salts (i.e., free of moisture, oxygen, or hydroxides) in chloride-based MSRs is important for a variety of factors, such corrosion and redox control.[20, 21]To remove impurities such as water, oxide ions, and hydroxide ions that would affect the chemistry of the salts, a LiCl-KCl (42 mol% KCl) eutectic was purified in a two-step process before conducting spectroscopic measurements. The salt purification system is based on the design by Choi et. al.[22] An image of the salt purification system is shown in Figure 2-1. A batch of 100 g salt was loaded into a high-purity alumina crucible placed inside a quartz vessel. Quartz wool was placed inside the top of the quartz reactor to prevent thermal shock. A Teflon lid with pre-cut holes was clamped to seal the quartz vessel, and a thermocouple inserted into a quartz wool was used to monitor temperature. An alumina tube was inserted into the reactor, allowing for the introduction of UHP Ar and/or anhydrous HCl gas into the headspace over the salt.

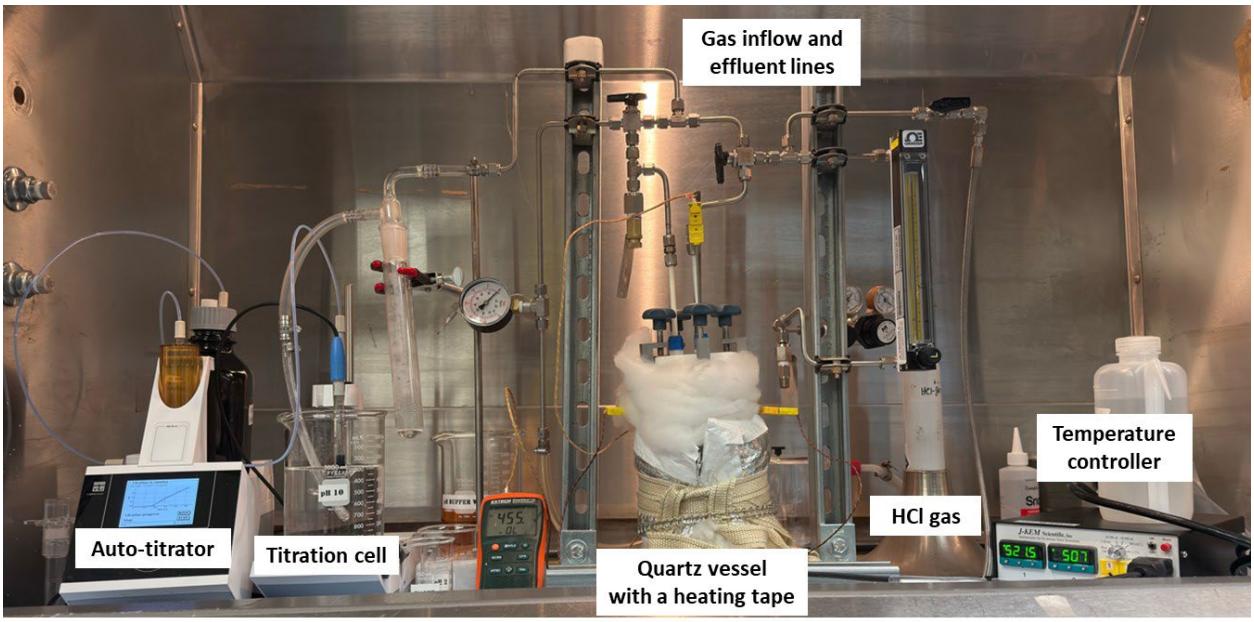

Figure 2-1. Photograph of salt purification system.

The first step in the purification process is dehydration. The vessel was evacuated, then heated to 200 °C at 250 °C/hr and held for 1 hour to remove moisture while under vacuum. The vessel was then heated to 500 °C at 250 °C/h, to melt the LiCl-KCl eutectic. The vacuum was then disconnected and replaced with UHP Ar gas flowing at 50 mL/min. Then, HCl gas (25% vol in UHP Ar) was flowed through the molten salt at 120 mL/min for up to 2 hrs. During this hydrochlorination phase of the salt treatment, the effluent gas coming out of the quartz reactor was bubbled into a titration cell connected to a TitroLine 7000 auto titrator running in pH Stat mode (pH=10) using 0.1 M NaOH as the titrant. The function of the auto titrator was to indicate the time at which there was no net HCl consumption in the vessel. When HCl stopped reacting with impurities, the quartz reactor was allowed to cool to room temperature with maintaining UHP Ar flow. The ramp rate was 30 °C/hr to prevent damage to the alumina crucible from temperature shock. An image of the purified salt is shown in Figure 2-2.

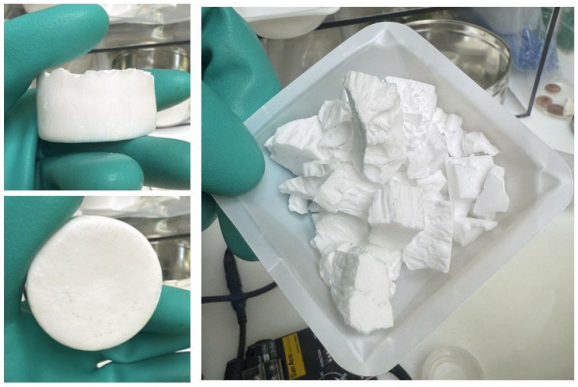

Figure 2-2. Photographs of purified LiCl-KCl salt pucks.

Figure 2-3 plots the consumed volume of 0.1 M NaOH vs. time curve during purification of the LiCl-KCl. The slope of the bypass was 0.01921, indicating that HCl was flowing directly into the auto-titration cell (green in Figure 2-3). The slope was reduced to 0.00201 when the HCl gas was introduced to the purification quartz vessel (blue in Figure 2-3). This shows that the HCl gas was reacting with impurities in the LiCl-KCl salt, such as oxide (Equation 2-1) and hydroxide (Equation 2-2). When the reaction was complete, the slope increased to 0.01383, which indicates that all the impurities within the salt had reacted with the HCl gas and the gas was now reacting with the NaOH in the auto-titration cell (red in Figure 2-3).

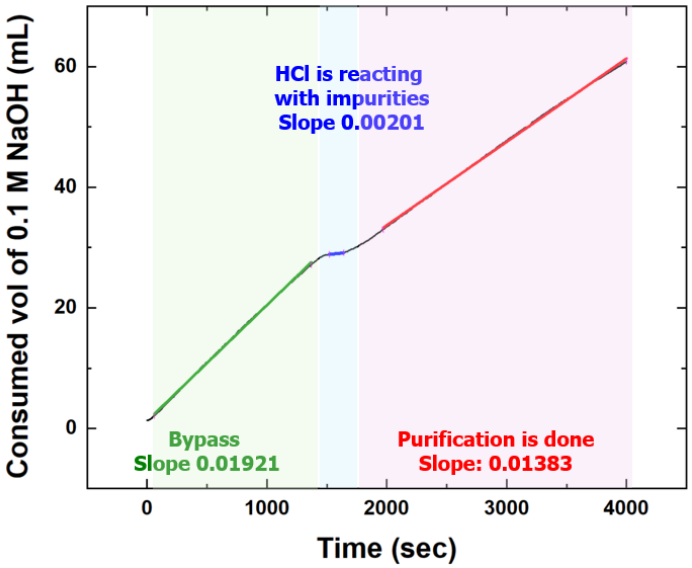

Figure 2-3. The consumed volume of 0.1 M NaOH vs time curve during purification process.

$$2HCl + 2O^{2-} \rightarrow H_2O + 2Cl^- \qquad \text{Equation 2-1}$$

$$HCl + OH^- \rightarrow H_2O + Cl^- \qquad \text{Equation 2-2}$$

The concentration of oxide and hydroxide cannot be distinguished from each other by acid-base titration; the total concentration is equivalent to concentration of OH^- plus half the concentration of O^{2-}. Thus, for simplification, the concentrations in this report are stated as concentration of OH^- but are in fact a combination of OH^- and O^{2-}. Acid-base titration was used to measure the concentration of hydroxide in the salt before and after purification. The auto-titrator runs in pH Stat mode (pH=2) using 0.1 M HCl as the titrant, and the minimum volume that the auto-titrator can measure is 1 µL. The detection limit of the auto-titrator is 1.00×10^{-7} moles. The samples were titrated three times each, and averages were calculated (Table 2-1). The concentration of unpurified salt and purified salt were 3.2×10^{-5} and less than 1.0×10^{-7}, respectively. This equates to two orders of magnitude reduction in the concentration after purification, which is at least 99.69% of the concentration of OH^-. The LiCl-KCl eutectic from Sigma Aldrich (AnhydroBeads) was analyzed to compare the concentration of purified salt. The purified salt produced here

has less OH^- than the purchased salt. Figure 2-4 shows the concentration of OH^- vs. unpurified salt, purified salt, and the purchased Sigma-Aldrich salt.

Table 2-1. The concentrations of the unpurified salt, purified salt, and purchased Sigma-Aldrich salt.

	OH^- moles/g		
	Before purification	After purification	Sigma Aldrich AnhydroBeads
1st	4.23×10^{-5}	0	3.03×10^{-6}
2nd	2.87×10^{-5}	0	3.03×10^{-6}
3rd	2.49×10^{-5}	0	3.06×10^{-6}
Avg.	3.20×10^{-5}	$<1.00 \times 10^{-7}$	3.04×10^{-6}
StDev	9.14×10^{-6}	Not applicable	1.78×10^{-8}

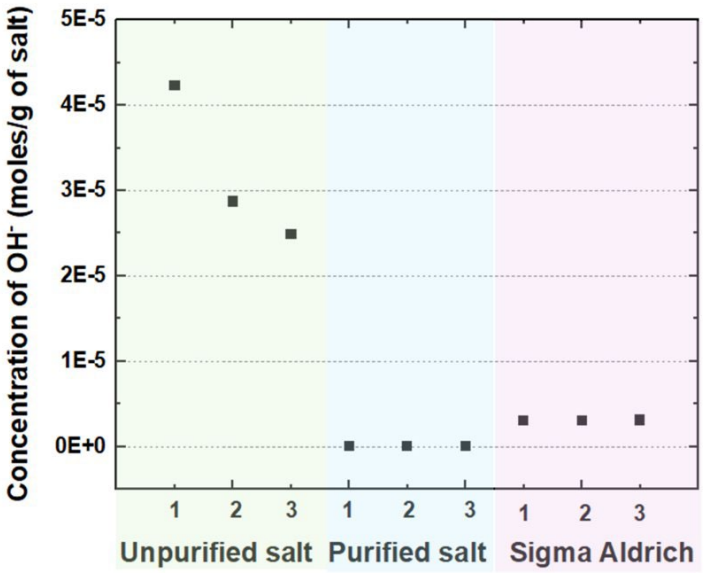

Figure 2-4. The concentration of OH^- vs. unpurified salt, purified salt, and the purchased Sigma-Aldrich salt.

2.4. Plutonium Chloride Synthesis

K_2PuCl_6 was synthesized in a non-inert glovebox from a stock of Na_2PuCl_6 synthesized previously on this project in FY24 (Figure 2-5). The Na_2PuCl_6 was dissolved in 2 M HCl solution while stirring at room temperature in a round-bottom flask. The dissolved Pu solution was then diluted with 5 M KOH, allowing the Pu to form as a fluffy, green $Pu(OH)_4$ precipitate (Figure 2-5A). The supernatant was pulled from above the $Pu(OH)_4$ solid layer. The dissolution with HCl and subsequent precipitation with KOH was repeated 2 more times. After the third precipitation with KOH and removal of the supernatant layer, the settled solids were dissolved with 2 M HCl while stirring. Anhydrous KCl was added to the solution to meet a K/Pu 2:1 molar ratio and allowed to dissolve, forming a greenish-yellow solution (Figure 2-5B). The amount of KCl added was chosen to make the theoretical ratio

of potassium needed to synthesize the coprecipitate K_2PuCl_6.[23] The flask containing the $PuCl_4$-KCl solution was setup with a distillation flask to remove liquids from the sample (Figure 2-5C). The sample was boiled in the distillation setup until a thick, red-brown sludge remained. The sludge was transferred to a weigh boat in two batches and allowed to air-dry in the glovebox (Figure 2-5D). The first batch shows a lighter color indicating an excess of KCl. The darker color of the second batch indicated a higher amount of K_2PuCl_6. Gamma energy analysis confirms 4.77 wt% Pu in Batch 1 and 21.0 wt % Pu in Batch 2. Initial experiments were conducted with the Batch 1 Pu material. These samples were treated with zirconium as described in Section 3.1. In order to more accurately measure a pure component spectrum of Pu, a stock of $PuCl_3$ was synthesized in an inert environment.

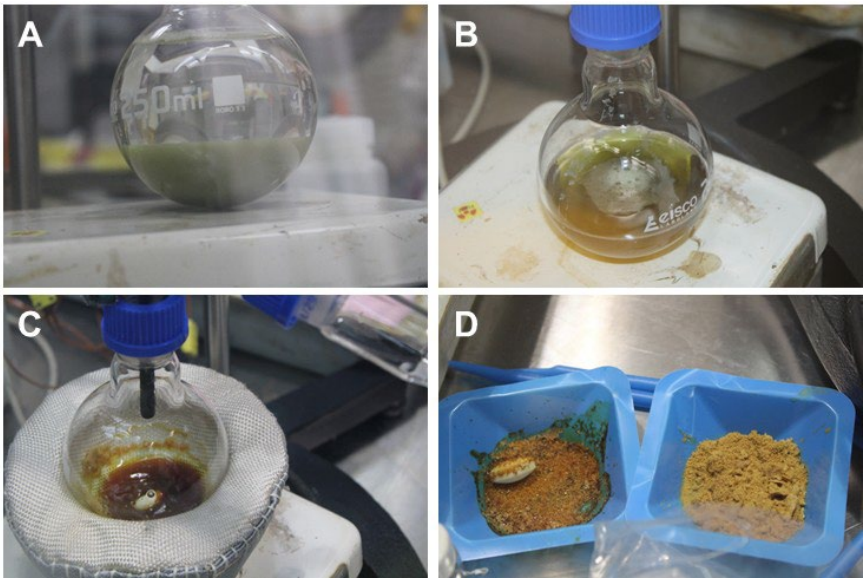

Figure 2-5. Photographs of Pu(IV) chloride synthesis: (A) $Pu(OH)_4$ solids in 5 M KOH; (B) $Pu(OH)_4$ and KCl dissolved in 2 M HCl; (C) distillation of K_2PuCl_6; (D) 4.77 wt% (Batch 1, right) and 21.0 wt% (Batch 2, left) K_2PuCl_6 in excess KCl.

To synthesize $PuCl_3$, ascorbic acid was added to a Pu(IV) nitrate solution to reduce the Pu(IV) to Pu(III). Oxalic acid was then added to the Pu solution to precipitate trivalent oxalate crystals, $Pu_2(C_2O_4)_2 \cdot 10H_2O$. The Pu(IV) sample contained <0.1% Am as determined by UV-vis spectroscopy. The precipitated Pu(III) oxalate material was washed with water followed by filtration and was subsequently washed with dry ethanol and methanol. The dried, blue material was immediately brought into an inert box. In the inert box, 0.219 g Pu(III) oxalate hydrate (Figure 2-6A) was weighed into a glassy carbon crucible and a 10-fold excess of freshly dried (250 °C, 18 hr) ammonium chloride was stirred into the crucible. The crucible was placed into a 2” outer diameter (OD), C276 material reactor and closed with a copper gasket. The reactor was removed from the inert box to a metal Schlenk line. A dry argon purge, set at 900 torr was passed into the reactor. The output flow was maintained with a needle valve to maintain the containment pressure near 900 torr. Tygon tubing was placed at the output of the needle valve. The reactor was heated to 200 °C for 2 hours to remove the waters of hydration from the Pu(III) oxalate

and then heated at 350 °C for 2 hours to initiate decomposition of the ammonium chloride. Ammonium chloride was detected at the output of the tubing by using a pH strip. The tubing output was placed into a poly bottle, in which reformed crystals of ammonium chloride were observed, whereas there were none on the walls of the tubing. Additionally, no Pu contamination was observed inside the poly bottle because of the slow flow rate achieved at the needle valve. The ammonium chloride emission continued, so the reactor was heated to 400 °C for 1 hour, at which point the ammonium chloride emission was slowed. Finally, the temperature was raised to 500 °C to fully expunge any excess ammonium chloride from the walls of the reactor (Figure 2-6B). A soft blue-green powder was removed from the crucible in the inert box (Figure 2-6C). The yield was 91.5% based on theoretical yield of the $PuCl_3$ from the oxalate. Some of the loss is due to handling in the glovebox and some may be due to differences in the initial mass of oxalate (water).

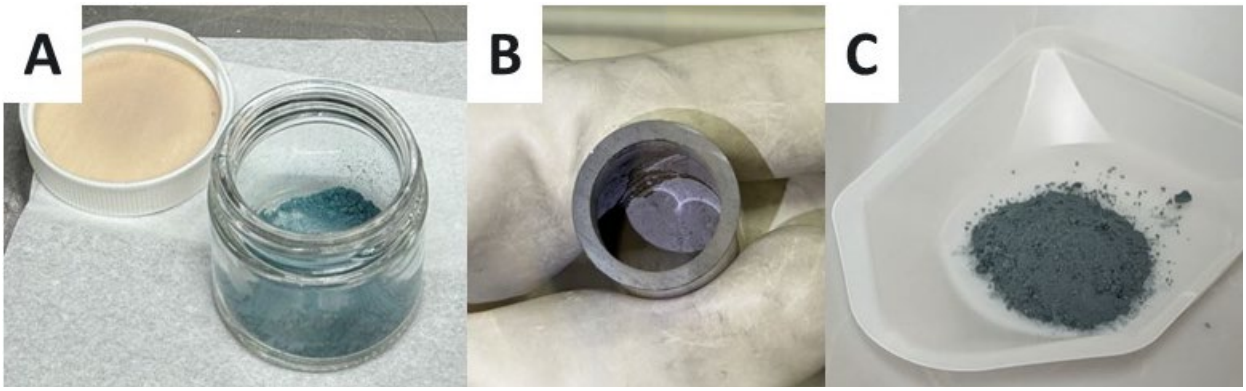

Figure 2-6. Photographs of Pu(III) chloride synthesis: (A) Pu(III) oxalate; (B) $PuCl_3$ after reaction with ammonium chloride in reactor vessel; (C) final $PuCl_3$ product.

2.5. Small-Scale Setup for MC&A Studies

The small-scale system developed for MC&A of target analytes is described in previous reports published under the Advanced Reactor Safeguards and Security (ARSS) campaign.[18, 24, 25] A visualization of the small-scale furnace system is shown in Figure 2-7. The furnace houses an optically transparent sample (cuvette) holder. The cuvette and holder have a long neck to provide a cold finger in order to prevent the molten salt from creeping out of the cuvette. The system allows for Raman and transmission spectroscopy to be recorded simultaneously.

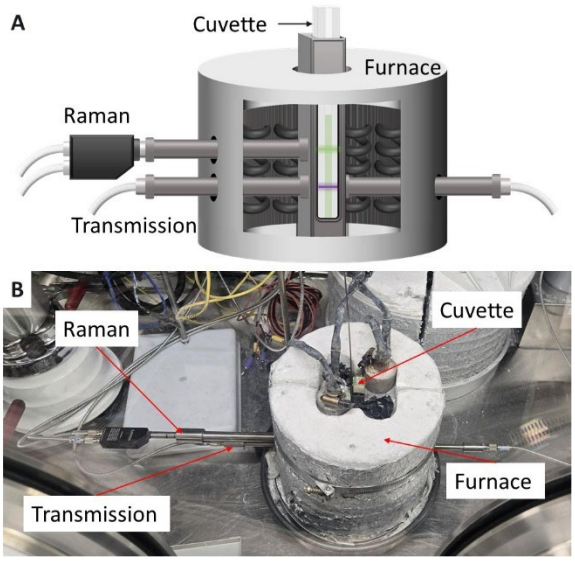

Figure 2-7. Small-scale furnace system: (A) schematic showing vessel inside a clam-shell furnace with both Raman and transmission optics to spectroscopic instruments; (B) photograph of small-scale furnace system.

In FY25, the transmission path was modified to collect both UV-vis and NIR. The ability to measure into the NIR allows for more information than UV-vis alone. Adding NIR can aid in quantifying species which have interfering or overlapping bands in the UV-vis range.

Raman, UV-vis, and NIR spectroscopic instruments were acquired from Spectra Solutions Inc., and each utilized a high throughput volume phase holographic grating spectrograph with a thermoelectrically-cooled two-dimensional charge-coupled device detector. The UV-Vis instrument had a functional wavelength range of approximately 450 – 850 nm. The NIR had a range of 900 – 1700 nm. The Raman instrument utilized a 532 nm excitation laser with a fiber optic Raman probe with a backscattering (180°) optical design. The wavenumber axis was calibrated using naphthalene and the resolution was <5 cm^{-1}. The wavenumber range is 140 – 4500 cm^{-1}.

Several measurements were performed on Pu and Nd in molten salts. These data were divided into a training set for model building and a validation set for determining the uncertainty of the models. The weight percent (wt%) concentration ranges for each set are shown in Table 2-2. Additional details on each data set will be provided in Section 3.

Table 2-2. Summary of training and validation set compositions.

Data Set	Pu, wt%	Nd, wt%
Training	0 – 0.5869	0 – 0.6660
Validation	0 – 0.7500	0 – 0.5146

2.6. Chemometric Analysis

Spectral data was collected using Spectra Soft software. These data were then extracted and analyzed using MATLAB (version 2022b) with the Eigenvector Research PLS-Toolbox (version 9.2.1). UV-vis and NIR spectral preprocessing included selection of certain wavelength ranges to remove light source artifacts, including the Raman laser line, followed by a polynomial baseline correction.

Partial least-squares (PLS) models were generated for Pu(III) and Nd(III) in the molten salts. Model statistics include the root-mean-square error of calibration (RMSEC) which provides the uncertainty in the calibration/training set. The root-mean-square error of cross validation (RMSECV) is the uncertainty of prediction for data sequentially left out of the model. The cross validation was a venetian blinds with 4 splits and blind thickness of 1. This means that on average, 25% of the training set was left out at a time during cross validation. The root-mean-square error of prediction (RMSEP) is a measure of uncertainty of the validation set which was not used in building the models.

3. RESULTS AND DISCUSSION

3.1. Proof of concept testing of Pu in molten chloride

The work completed in these studies utilized two different sources: Pu(IV) with known waters of hydration and an anhydrous Pu(III) synthesized in an inert environment.[24] The Pu(IV) was faster to acquire since the group already possessed the $PuCl_4$-NaCl stock from FY24 work to determine repeatability of the spectral fingerprint collection. Figure 3-1 shows a spectrum of the Pu(III) in a molten NaCl-$MgCl_2$ eutectic. This spectrum shows the characteristic peaks at 568 nm, 604 nm, 672, nm and 798 nm, which are consistent with the literature values shown in Table 3-1.

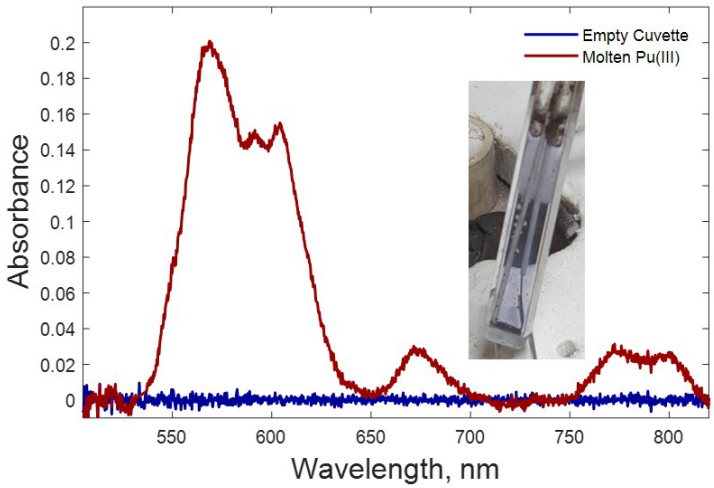

Figure 3-1. Spectra of 0.75 wt% Pu(III) in NaCl-$MgCl_2$ at 550 °C collected in FY24 used to determine molar absorptivity of Pu(III) with inset photograph of Pu(III) in molten NaCl-$MgCl_2$ at 550 °C.

The measurement of Pu from this work saw the full dissolution of the Pu(IV) solid in the form of Pu(III) in the molten NaCl-$MgCl_2$. This supports findings that the Pu species is more stable in the +3 oxidation state in molten chloride[26], which is crucial information for the operation of liquid fuel MSRs.

Work this FY saw the transition from a NaCl-$MgCl_2$ to a LiCl-KCl background eutectic for all measurements. This was due in large part to measure key targets in a eutectic chloride with a validated purity with regards to hydration (i.e., water, hydroxides). Through collaboration with other research groups, a non-radioactive salt purification system was built in the PNNL Radiochemical Processing Laboratory. The purification of the LiCl-KCl eutectic is detailed in Section 2.3.

Initial testing of the purified LiCl-KCl took place with the Pu(IV) solid. As described in Section 2.4, it was known that this Pu(IV) stock would contain waters of hydration and would likely lead to the formation of a Pu oxide or Pu oxychloride species. In the FY24 measurement, this was mitigated by the presence of a tungsten wire in the molten liquid. The measurements below utilize a Zr^0/Zr^{4+} system to mitigate the formation of an oxygen-containing Pu species. The chlorination of Pu in LiCl-KCl is shown in Figure 3-2. Upon the addition of the Pu(IV) (0.59 wt% Pu) to the molten LiCl-KCl, the analyte settled as a brownish-yellow heel in the bottom of the cell (Figure 3-3A). A slight increase was observed in the spectra where the Pu(III) fingerprint is expected (Figure 3-2A). To encourage dissolution/chlorination of the suspected Pu heel, Zr was added as Zr wire (Figure 3-3B) and $ZrCl_4$ (Figure 3-3C). The mechanism for chlorination is shown in Equation 3-1 and Equation 3-2, as found in literature.[27] After addition of the $ZrCl_4$, the sample showed an intense yellow color (Figure 3-3C). The spectra showed an increase in signal between 500 – 625 nm. This window includes some mixed analyte species that overlay the Pu(III) fingerprint. Over time (~36 hours), the large shoulder around 500 nm began to decrease (Figure 3-2B), leaving the fingerprint unique to Pu(III) (Figure 3-2A). After reaction with the Zr was complete, the sample showed a very dark blue color consistent with Pu(III) (Figure 3-3D).

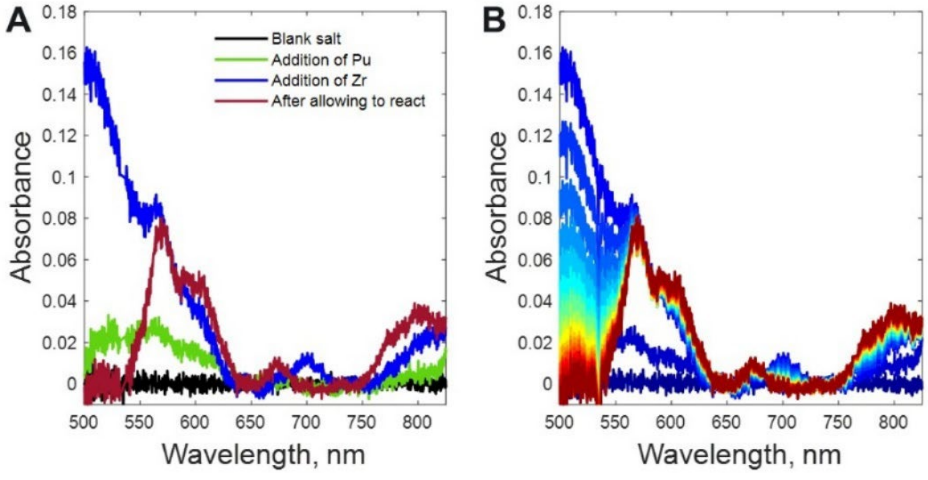

Figure 3-2. (A) Spectra collected at each major step for Pu(IV) reduction to Pu(III) by Zr in LiCl-KCl eutectic at 500 °C (B) Spectra collected throughout the reaction of Pu with Zr.

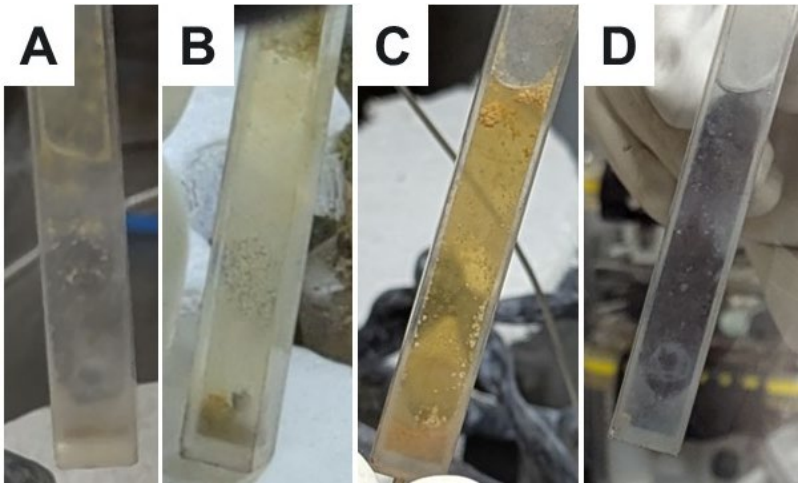

Figure 3-3. Photographs of Pu chlorination with Zr: (A) 0.3 wt% Pu solid in molten LiCl-KCl; 0.59 wt% Pu with Zr wire; (C) initial reaction of 0.59 wt% Pu with Zr wire and $ZrCl_4$; (D) 0.59 wt% Pu after reaction with Zr.

$$4PuO_2 + Zr + ZrCl_4 \rightarrow 4PuOCl + 2ZrO_2 \qquad \text{Equation 3-1}$$

$$2PuOCl + ZrCl_4 \rightarrow 2PuCl_3 + ZrO_2 \qquad \text{Equation 3-2}$$

Molar absorptivity values were compared for Pu(III) in the NaCl-$MgCl_2$ at 550 °C (Figure 3-1) to the Pu(III) in the LiCl-KCl eutectic at 500 °C (Figure 3-2). The values for each characteristic peak are listed in Table 3-1. The molar absorptivity values determined in this work are consistent with the information about similar systems in the literature. Note that differences between molar absorptivities across systems can be caused by salt composition, temperature, and differences in densities used in the calculation of molar concentrations. The densities used for this work are 2.018 g/cm^3 for NaCl-$MgCl_2$ and 1.614 g/cm^3 for LiCl-KCl.[28] For the purposes of this work, wt% concentrations will be used from here on as a more representative concentration unit for industrial processes.

Table 3-1. Molar absorptivities for each major Pu(III) peak in the visible region compared to previously reported values.

Source	Solvent	ε_λ (L·mol^{-1}·cm^{-1})						T (°C)
		568	589	604	671	772	790	
Barbanel[29]	LiCl-KCl	14	9					400
Swanson[30]	LiCl-CsCl	10						400
Lambert[31]	LiCl-KCl	12.08	8.15	---	1.74	---	4.27	450
Bamberger[32]	LiF-BeF_2-ThF_4	20						575
This work	**NaCl-$MgCl_2$**	**16.6**	**11.4**	**11.7**	**2.2**	**2.4**	**2.1**	**550**
This work	**LiCl-KCl**	**22.3**	**15.0**	**13.7**	**3.2**	**6.7**	**9.2**	**500**

3.2. Chemometric modeling of Pu(III) and Nd(III)

The data collected in Figure 3-2B was used as the training set for Pu(III), as multiple concentrations of Pu(III) could be determined throughout the reduction with Zr. The first analysis that was performed was a multivariate curve resolution (MCR) to deconvolute the spectral components in the system. The analysis results are shown in Figure 3-4. The analysis revealed 2 components: one which encompasses the shoulder centered at ~550 nm decreasing over time, and one that is the Pu(III) signature centered at ~575 nm increasing over time. This is consistent with an oxidation state change in Pu during the reduction with Zr.

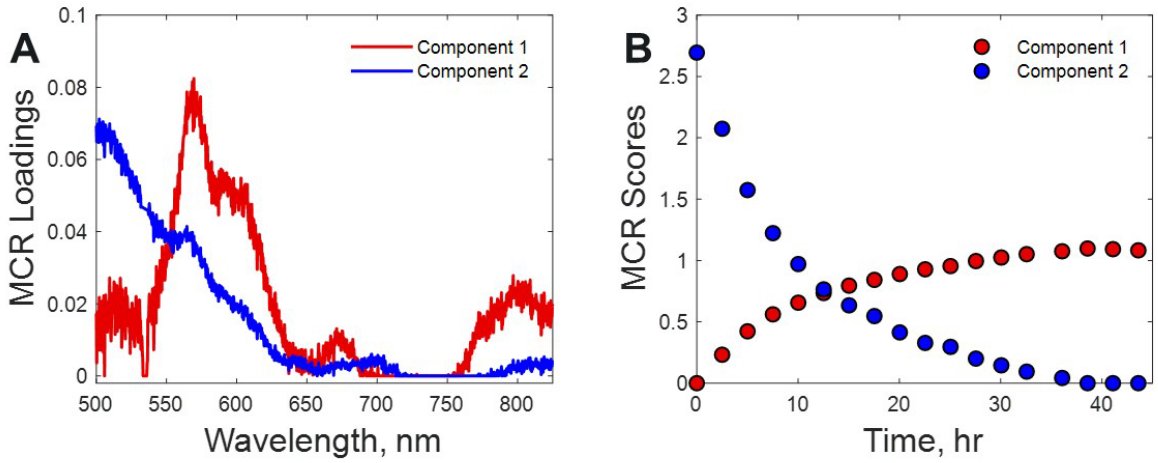

Figure 3-4. MCR analysis results showing (A) the spectra for each component and (B) the relative amounts of each component over time.

The results in Figure 3-4 indicate that the reaction reached steady-state by the end of the experiment, as the amounts of each component stabilized. These results also show that the Pu(III) signature in Figure 3-2B is increasing over time even though the spectrum appears to be constant. This is because the Pu(III) signature overlaps with the shoulder at 550 nm. If the Pu(III) signature was actually constant (i.e., the Pu(III) concentration was constant), then the Pu(III) signature at 575 nm would be on top of the shoulder at 550 nm.

This led to additional analysis where a baseline was applied to remove the shoulder at 550 nm and reveal the Pu(III) signature at 575 nm. The results of this baseline correction are shown in Figure 3-5A. Considering the reaction appears to have reached steady state, it was therefore concluded that all of the Pu reacted to form Pu(III). Knowing the total Pu(III) added to the salt (0.5869 wt%), the concentrations of each spectrum in Figure 3-5A were calculated based on the Beer-Lambert Law. These calculated concentrations were plotted against the baseline corrected peak absorbances at 568 nm and are shown in Figure 3-5B. From the slope of the fitted line (m) and the noise of the blank measurement(s), the limit of detection (LOD) was calculated as 0.019 wt% using Equation 3-3.

$$\mathrm{LOD} = \frac{3s}{m}$$ Equation 3-3

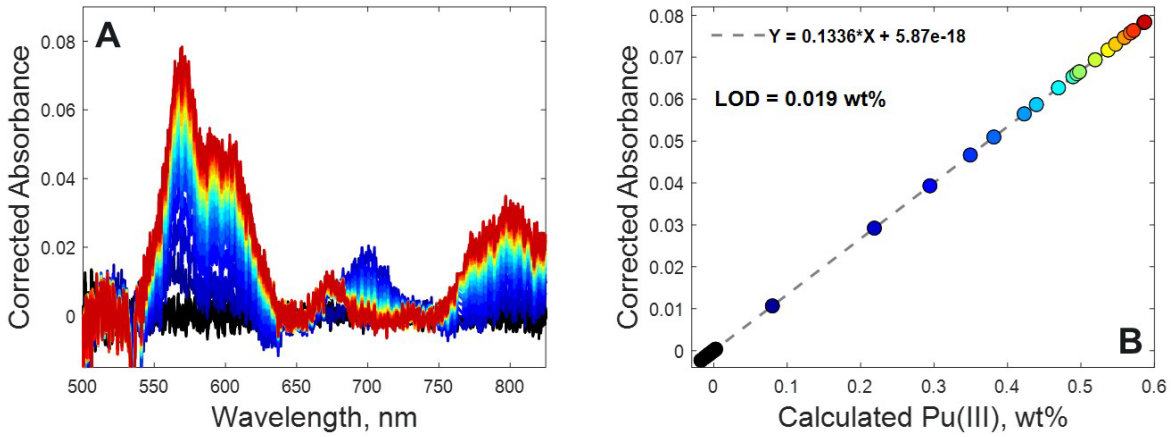

Figure 3-5. (A) Baseline corrected spectra from Figure 4-3B. (B) LOD calculation from the calculated Pu(III) concentration vs. baseline corrected absorbance at 568 nm.

The spectra in Figure 3-2B along with the Pu(III) concentration values were then used as the training set in the PLS model for Pu(III). Neodymium (Nd) spectra collected in the same eutectic were also added to the training set to allow the model to distinguish between Pu(III) and Nd(III) which have overlapping bands. The training set spectra are shown in Figure 3-6A. The validation set consisted of the Pu(III) spectra in Figure 3-1 corrected for a different pathlength, as well as additional Nd(III) spectra collected in a separate experiment. The validation set spectra are shown in Figure 3-6B. Both Pu(III) and Nd(III) models were developed, and the results are shown in Figure 3-6 C and D. These parity plots show the Pu(III) and Nd(III) concentration vs. the model measured concentrations. A 1:1 correlation indicates a good model. The predicted concentration of the validation set is also plotted. These independent measurements fall within the 95% confidence intervals indicating accurate models.

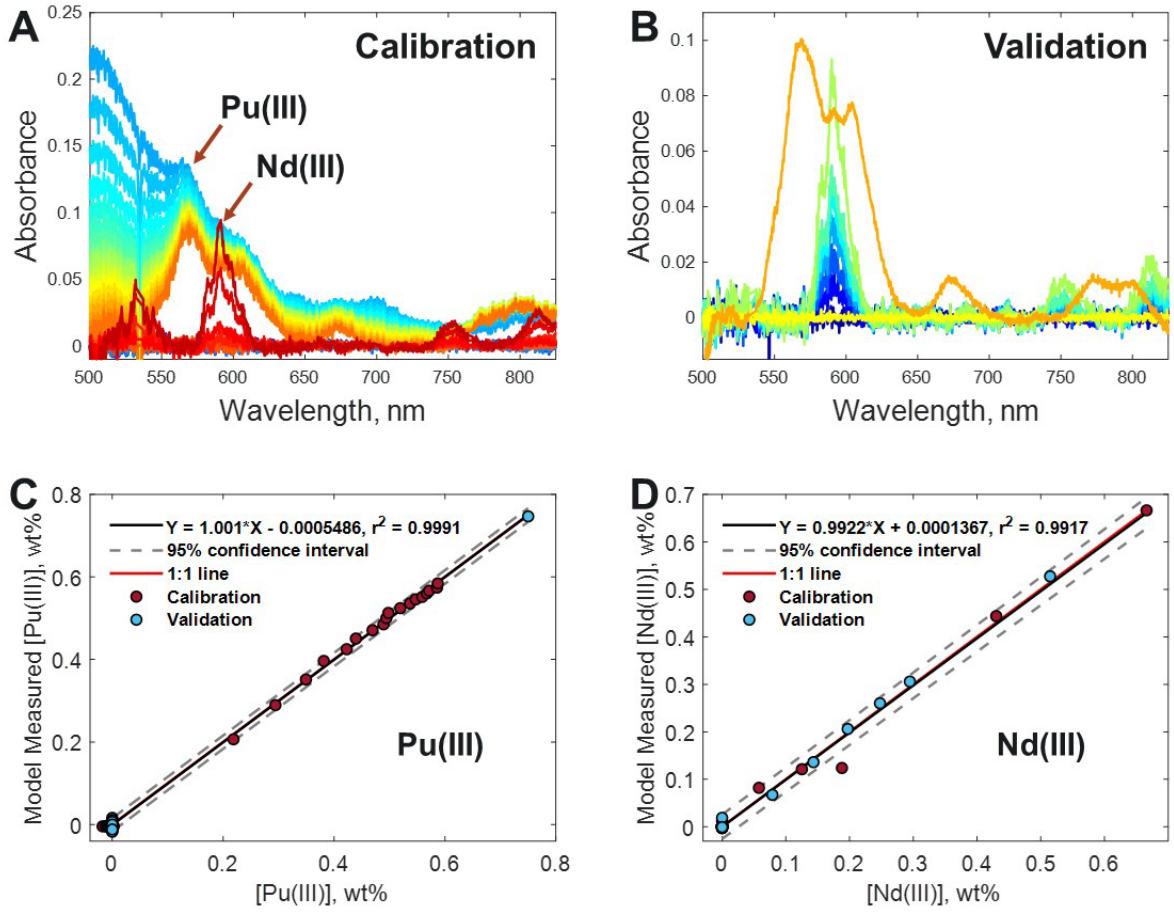

Figure 3-6. (A) Training set spectra. (B) Validation set spectra. (C) Model results for Pu(III). (D) Model results for Nd(III).

The model statistics are shown in Table 3-2 along with the percent uncertainty calculated from the total concentration range studied. Overall, the RMSEC values are smaller than the RMSECV values, which is expected as the RMSEC takes into account the entire training set, while the RMSECV is the uncertainty of data systematically removed from the dataset during cross validation. The RMSEP values, which are the uncertainty of the independent validation set, are similar to the RMSEC and RMSECV values indicating good model predictions. All the model statistics for Pu(III) and Nd(III) range from 1.3 – 2.2%.

Table 3-2. Model statistics for Pu(III) and Nd(III) along with the percent uncertainty of the total concentration range studied.

Model Statistics	Pu Uncertainty, wt%	Pu % Uncertainty	Nd Uncertainty, wt%	Nd % Uncertainty
RMSEC	0.00753	1.3	0.0123	1.8
RMSECV	0.00835	1.4	0.0148	2.2
RMSEP	0.0100	1.7	0.0109	1.6

Additional studies were performed which involved mixtures of Pu and Nd in molten LiCl-KCl. These were done to test the models' ability to distinguish between different interfering species in the melt. The first experiment began with a melted blank LiCl-KCl eutectic. Analytes salts were added to the sample melt by pressing a small mass into a pellet using a handheld pellet press. A pellet of $PuCl_3$ was added to the salt and allowed to dissolve. This was followed by two pellets of $NdCl_3$, and finally a second pellet of $PuCl_3$. The PLS models for Pu(III) and Nd(III) were applied to these data and the results are shown in Figure 3-7. The spectra in Figure 3-7A and B show the overlapping Pu and Nd peaks growing in over the course of the experiment. Figure 3-7C shows the model results for Pu and Nd. At the start of the experiment, both models accurately predicted zero Pu and Nd in the blank salt. After the first addition of Pu, the predicted concentration of Pu increased while Nd remained at zero. After the second addition of Nd, there was an increase in the predicted concentration of Nd and a slight decrease in Pu, consistent with dilution. The same trend was observed after the second addition of Nd. After the final addition of Pu, there was a more gradual increase in the Pu concentration and a slight decrease in Nd, again consistent with dilution. Immediately after the second addition of Pu, both models also predicted anomalous values (lower Pu and higher Nd concentrations) which could be caused by solids temporarily blocking the light path. The gradual increase in Pu following this dip is also consistent with slower dissolution of Pu in the salt.

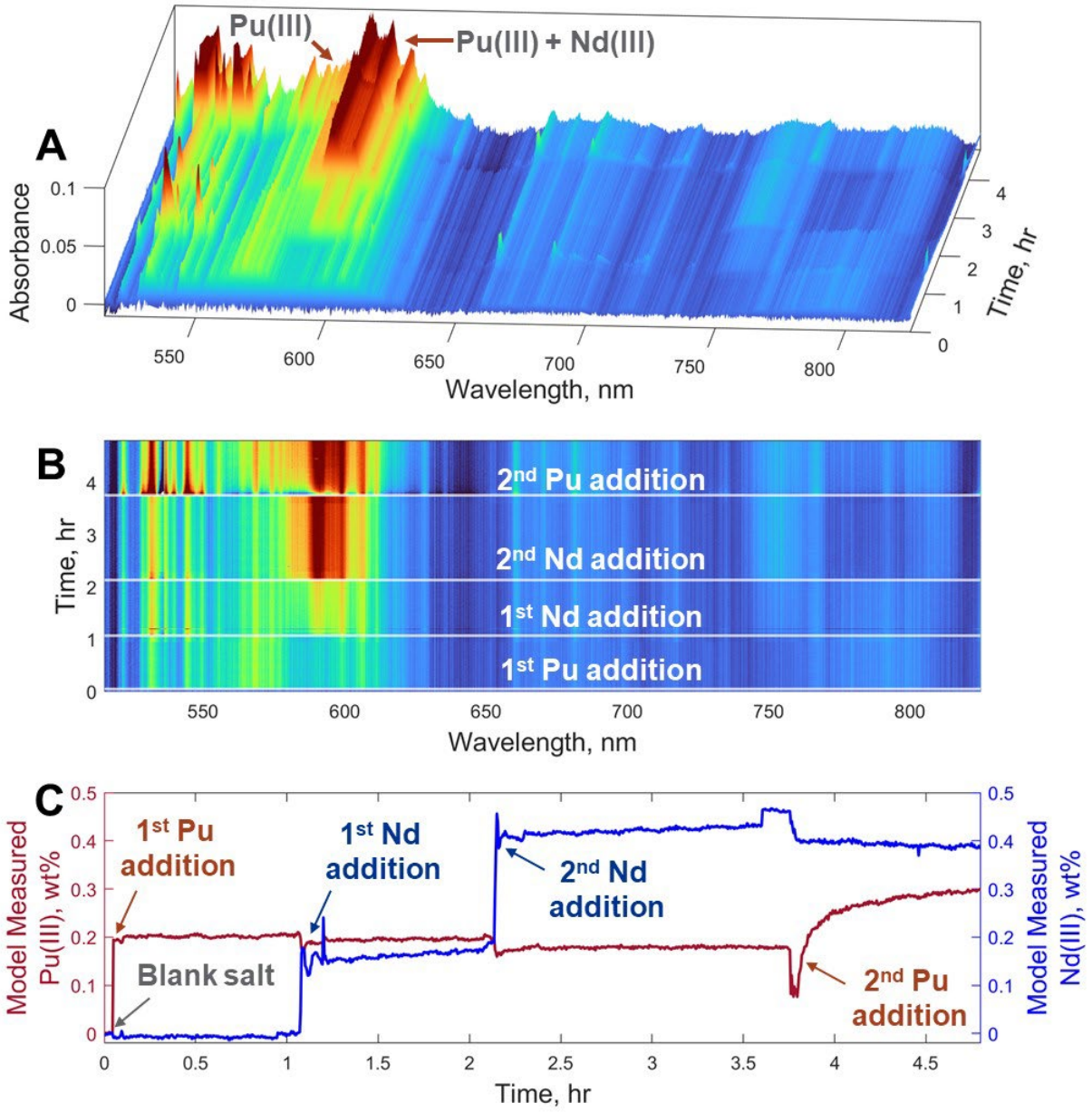

Figure 3-7. Spectra taken over the course of Pu and Nd additions shown as (A) a surface plot over time and (B) top-down surface plot showing time-points of each addition. (C) Model results of Pu(III) and Nd(III) concentration over time.

The second experiment started with Pu already mixed into the LiCl-KCl eutectic. In this experiment, two pellets of Nd were added after the Pu salt melted. The results are shown in Figure 3-8. In this experiment, the model results are noisy at the start of the experiment as the melting salt came to equilibrium. The concentration of Pu then stabilized over time. After each addition of Nd, the Pu concentration was predicted to decrease slightly, consistent with dilution, while the Nd model predicted increasing concentrations of Nd.

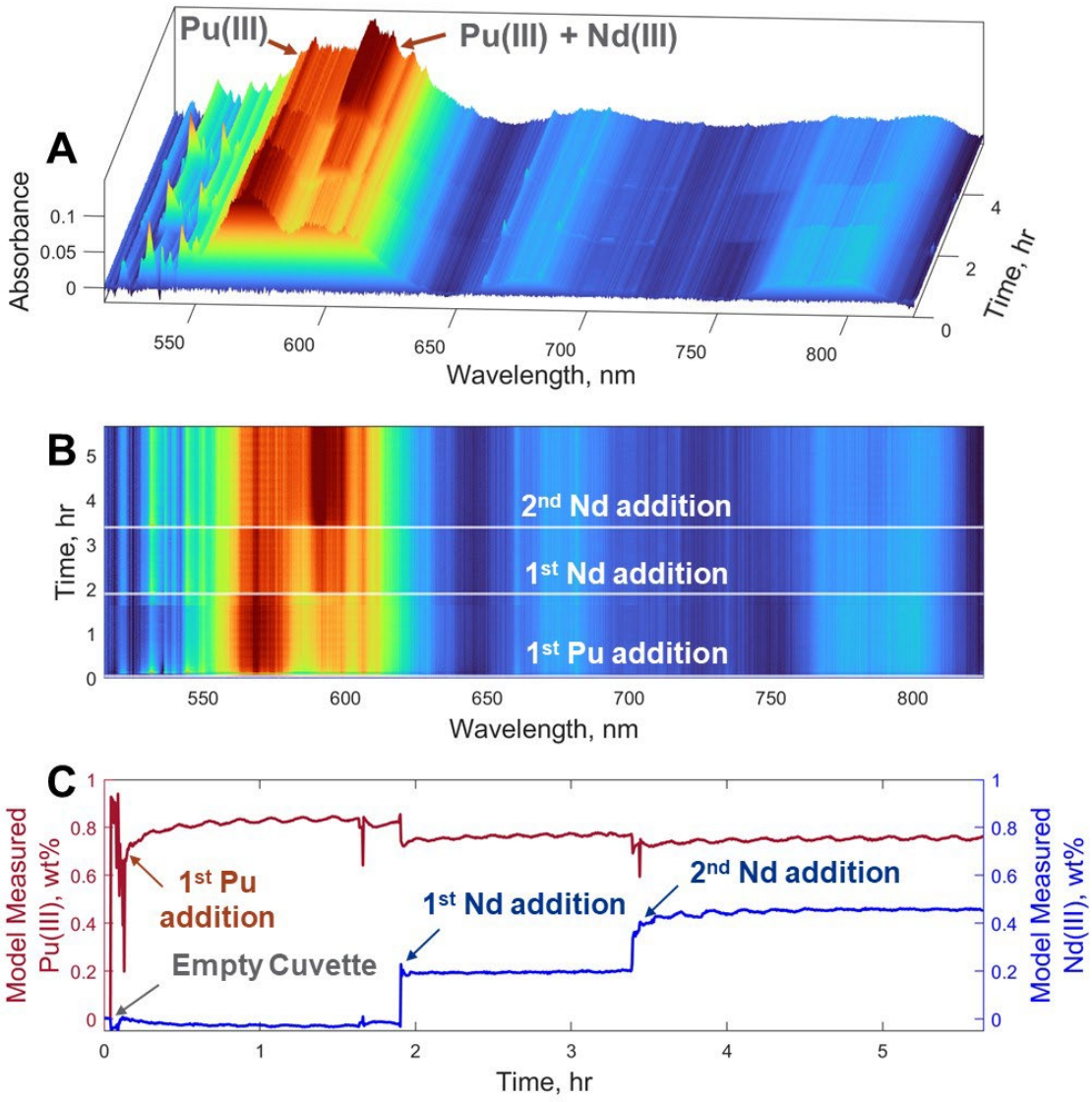

Figure 3-8. Spectra taken over the course of Pu and Nd additions shown as (A) a surface plot over time and (B) and top-down surface plot showing each addition. (B) Model results of Pu(III) and Nd(III) concentration over time.

Both of these mixed analyte experiments show the ability for chemometric models to distinguish between overlapping and interfering species. This demonstration also shows the value in continuous monitoring of salt composition over time. It is important to note the models in Figure 3-7 and Figure 3-8 are able to monitor the amount of dissolved Pu and Nd. As the Pu added to these samples did not fully dissolve, the model results cannot be compared to known concentrations. However, the accuracy of the pure analyte Pu model (Figure 3-6C) – where it is known that all Pu dissolved – gives confidence that the model is able to accurately quantify the amount of dissolved Pu. Additionally, it is very

important to emphasize that the model is able to distinguish between Pu(III) and Nd(III), which have overlapping optical fingerprints in the UV-vis region.

3.3. Expansion into NIR and Raman

Incorporating additional sensors into a process can improve the identification and quantification of different species. In this work, Pu(III) shows both UV-vis and NIR fingerprints. A comparison of these fingerprints is shown in Figure 3-9. The NIR peaks identified here are consistent with previous work.[30]

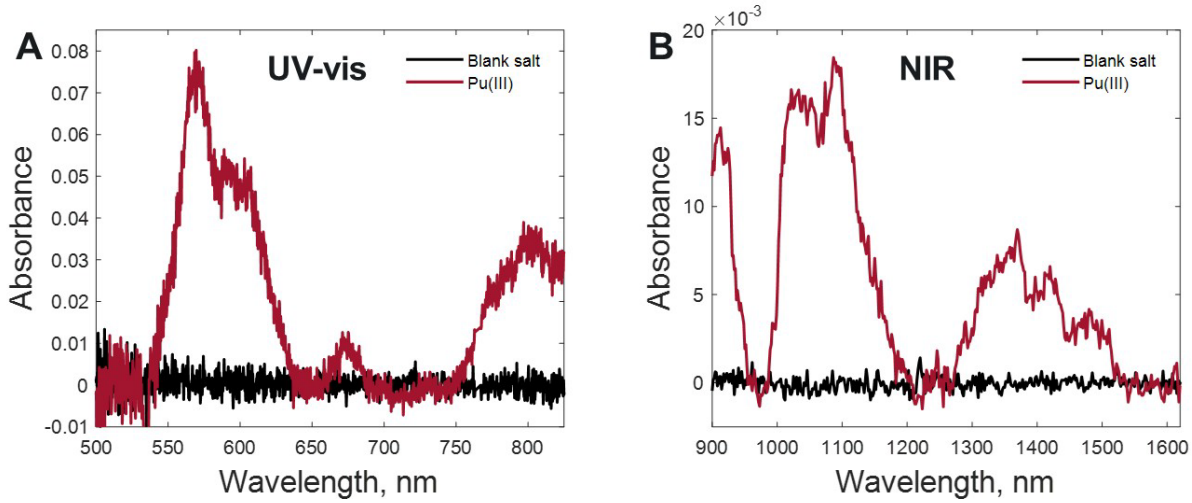

Figure 3-9. Spectra of blank LiCl-KCl salt and 0.59 wt% Pu(III) collected on the (A) UV-vis system and (B) NIR system.

The sections above demonstrated the ability for chemometric models to distinguish and quantify multiple interfering species in a chemical system. Additionally, pairing multiple optical sensors can improve this analysis, which can be helpful in more complex mixtures. For this work, Nd(III) was chosen as an interfering species because the primary Nd(III) UV-vis absorbance peak overlaps with the primary Pu(III) peak. Nd, however, does not have significant NIR peaks. For Raman spectroscopy in molten salts, Pu(III) does not have a significant Raman signature, but Nd(III) has a prominent fluorescence spectral fingerprint that was measured by Raman.[33] A comparison of Pu(III) and Nd(III) fluorescence/Raman fingerprints are shown in Figure 3-10. By pairing multiple spectroscopic techniques, identifying certain analytes becomes easier and the uncertainty of the models can improve. Future work will move towards data fusion with these various techniques to more accurately measure analyte concentration.

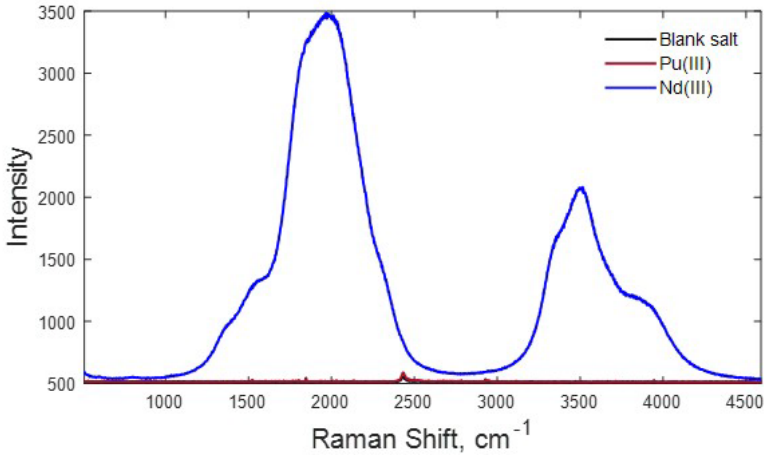

Figure 3-10. Raman measurement of a blank LiCl-KCl salt and ~0.6 wt% Pu(III) and Nd(III) showing the fluorescence of Nd(III).

3.4. Temperature effects

The team is beginning to explore the impacts of temperature on the optical Pu signatures. Optical fingerprints are expected to change with temperature as salt density changes and chemical speciation changes. The team integrated a summer SULI student this year to begin collecting variable temperature data. Some trends were observed, especially in the NIR region as a result of changes in temperature. The team is starting to analyze this data and plan for future experiments to explore potential impacts to chemometric modeling and how to make the models robust enough to handle temperature effects.

3.5. Advancing optical cells

In FY25, another advancement was the procurement of sapphire cuvettes. The cuvettes used in this work have been made of fused silica. While these have, for the most part, held up to the molten salt environment, they tend to become weakened or etched over time. Reheating cuvettes can lead to cracking, meaning that most of the time, these cuvettes are only single use. A more economical option was in procuring cuvettes which are made of a more robust material. Sapphire is potentially a better option as it is more corrosion resistant while remaining optically transparent. Initial testing of these cuvettes was performed in the aqueous phase before the cuvettes would be brought into the inert box. The UV-vis, NIR, and Raman testing results are shown in Figure 3-11. To assess each technique, different analytes were chosen to provide the best optical signal.

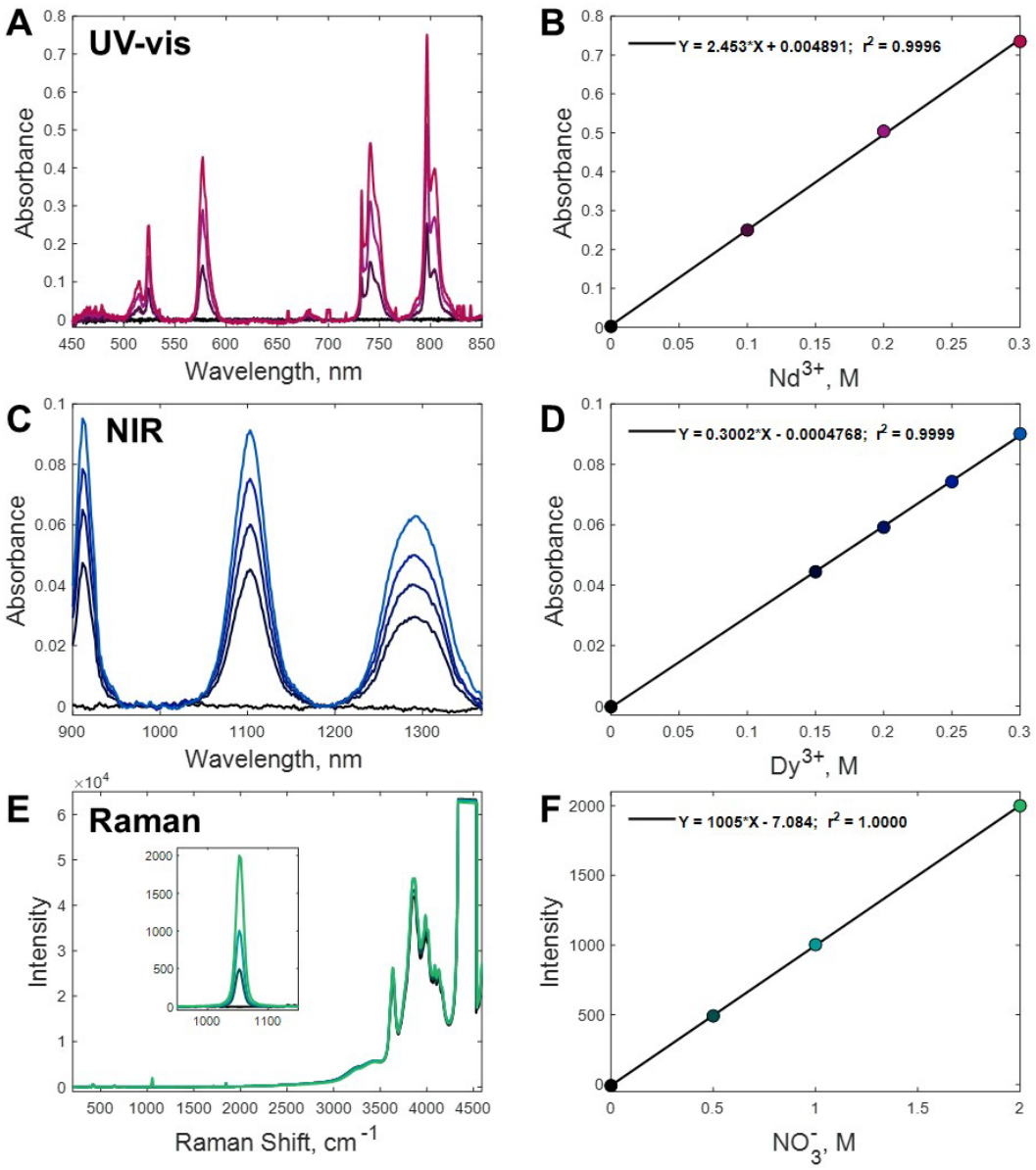

Figure 3-11. (A) $Nd(Cl)_3$ measured on the UV-vis system with the corresponding (B) calibration curve for the peak at 796 nm. (C) $Dy(Cl)_3$ measured on the NIR system with the corresponding (D) calibration curve for the peak at 1102 nm. (E) $NaNO_3$ solutions measured on the Raman system with the corresponding (F) calibration curve for the nitrate peak at 1052 cm^{-1}.

Overall, the sapphire cuvette performed well for UV-vis and NIR spectroscopy. The Raman spectra, however, did show interference from fluorescence of the sapphire. This fluorescence was most significant in the higher wavenumber range above ~3500 cm^{-1}. For this work, most Raman active analytes of interest such as uranyl and plutonyl would have Raman bands in the lower region <1000 cm^{-1}.[16, 34, 35] This cell fluorescence can also be mitigated by changing the wavelength of the excitation laser.

4. CONCLUSION AND RECOMMENDATIONS

Optical spectroscopy tools continue to demonstrate valuable applicability to on-line monitoring of key MC&A targets within molten salts. In FY25, the PNNL team demonstrated the capability to quantify Pu within molten chloride salts containing Pu and Nd as a representative interferent. This included integrating three types of optical spectroscopy: vis and NIR absorbance and Raman spectroscopy. Multiple Pu bearing salts were characterized, exploring different ranges of Pu concentration, oxidation state, the presence of different intensities of interfering signals, and temperature ranges for the salt melt. Data was used to build and validate performance of chemometric models for Pu quantification, which performed well in subsequent tests where melt conditions were varied. The uncertainty of the Pu(III) quantification model was 0.01 wt% (< 2%).

The PNNL team continued to advance their small-scale molten salt system design to allow for optimized testing and characterization of molten salts while testing and using materials that would be expected for use in sensors in larger-scale salt systems. This included improving furnace design, improving optics integration, and utilizing cell materials that correspond to sensor window materials.

Additionally, the PNNL team continues to look for opportunities to collaborate with industry partners to better understand monitoring needs and limitations while exploring options to test or validate sensors on relevant systems. PNNL has had a long-standing interaction with TerraPower that resulted in the sharing of salts in previous FYs, and the team hopes to continue and expand these connections. The team also integrated a SULI student for the summer of FY25.

Overall, FY25 demonstrations indicate optical spectroscopy-based tools can play a key role in supporting effective MC&A within molten salt systems. Ideally, optical tools will provide one piece of the comprehensive input needed and can support continuous insight into reactor trends by providing detailed chemical information (e.g., speciation, oxidation state, etc.). Recommended next steps include exploring and advancing abilities to fuse multiple data streams for more robust and flexible MC&A of molten salt systems.

5. ACKNOWLEDGMENTS

This work was funded by the Department of Energy Office of Nuclear Energy's Advanced Reactor Safeguards Campaign. Pacific Northwest National Laboratory (PNNL) is operated by Battelle Memorial Institute for the DOE under contract DE-AC05-76RL01830.

6. REFERENCES

(1) Branch, S. D.; Felmy, H. M.; Arbova, D. L.; Batie, G.; Good, E. C.; Bryan, S. A.; Lines, A. M. Data Fusion: Applying Chemometric Modeling to Gamma and Optical Spectroscopic Data, PNNL-37731. Laboratory, P. N. N., Ed.; Richland, WA, 2025.
(2) Schroll, C. A.; Lines, A. M.; Heineman, W. R.; Bryan, S. A. Absorption spectroscopy for the quantitative prediction of lanthanide concentrations in the 3LiCl-2CsCl eutectic at 723 K. *Analytical Methods* **2016**, *8* (43), 7731-7738, 10.1039/C6AY01520D. DOI: 10.1039/c6ay01520d.
(3) Schroll, C. A.; Chatterjee, S.; Levitskaia, T. G.; Heineman, W. R.; Bryan, S. A. Electrochemistry of Europium(III) Chloride in 3 LiCl - NaCl, 3 LiCl - 2 KCl, LiCl - RbCl, and 3 LiCl - 2 CsCl Eutectics at Various Temperatures. *Journal of the Electrochemical Society* **2017**, *164* (8), H5345-H5352. DOI: 10.1149/2.0521708jes.
(4) Schroll, C. A.; Chatterjee, S.; Levitskaia, T. G.; Heineman, W. R.; Bryan, S. A. Electrochemistry and Spectroelectrochemistry of europium(III) chloride in 3LiCl-2KCl from 643 to 1123 K. *Anal Chem* **2013**, *85* (20), 9924-9931. DOI: 10.1021/ac402518p From NLM PubMed-not-MEDLINE.
(5) Schroll, C. A.; Chatterjee, S.; Levitskaia, T.; Heineman, W. R.; Bryan, S. A. Spectroelectrochemistry of EuCl3 in Four Molten Salt Eutectics; 3 LiCl-NaCl, 3 LiCl-2 KCl, LiCl-RbCl, and 3 LiCl-2 CsCl; at 873 K. *Electroanalysis* **2016**, *28* (9), 2158-2165. DOI: 10.1002/elan.201600048.
(6) Polovov, I. B.; Volkovich, V. A.; Charnock, J. M.; Kralj, B.; Lewin, R. G.; Kinoshita, H.; May, I.; Sharrad, C. A. In situ spectroscopy and spectroelectrochemistry of uranium in high-temperature alkali chloride molten salts. *Inorg Chem* **2008**, *47* (17), 7474-7482. DOI: 10.1021/ic701415z.
(7) Park, Y. J.; Bae, S. E.; Cho, Y. H.; Kim, J. Y.; Song, K. UV-vis absorption spectroscopic study for on-line monitoring of uranium concentration in LiCl-KCl eutectic salt. *Microchemical Journal* **2011**, *99* (2), 170-173. DOI: 10.1016/j.microc.2011.04.013.
(8) Nagai, T.; Uehara, A.; Fujii, T.; Yamana, H. Reduction behavior of UO_2^{2+} in molten LiCl-RbCl and LiCl-KCl eutectics by using tungsten. *Journal of Nuclear Materials* **2013**, *439* (1-3), 1-6. DOI: 10.1016/j.jnucmat.2013.03.078.
(9) Skutnik, S. E.; Sobel, P. W.; Swinney, M. W.; Hogue, K. K.; Arno, M. M.; Chirayath, S. S. Survey of prospective techniques for molten salt reactor feed monitoring. *Annals of Nuclear Energy* **2024**, *208*, 110796. DOI: 10.1016/j.anucene.2024.110796.
(10) Bryan, S. A.; Levitskaia Tatiana, G.; Johnsen, A. M.; Orton, C. R.; Peterson, J. M. Spectroscopic monitoring of spent nuclear fuel reprocessing streams: an evaluation of spent fuel solutions via Raman, visible, and near-infrared spectroscopy. In *Radiochimica Acta International journal for chemical aspects of nuclear science and technology*, 2011; Vol. 99, p 563.
(11) Lines, A. M.; Hall, G. B.; Asmussen, S.; Allred, J.; Sinkov, S.; Heller, F.; Gallagher, N.; Lumetta, G. J.; Bryan, S. A. Sensor Fusion: Comprehensive Real-Time, On-Line Monitoring for Process Control via Visible, Near-Infrared, and Raman Spectroscopy. *ACS Sens* **2020**, *5* (8), 2467-2475. DOI: 10.1021/acssensors.0c00659 From NLM Medline.
(12) Lines, A. M.; Hall, G. B.; Sinkov, S.; Levitskaia, T.; Gallagher, N. B.; Lumetta, G. J.; Bryan, S. A. Overcoming Oxidation State-Dependent Spectral Interferences: Online Monitoring of U(VI) Reduction to U(IV) via Raman and UV-vis Spectroscopy. *Industrial & Engineering Chemistry Research* **2020**, *59* (19), 8894-8901. DOI: 10.1021/acs.iecr.9b06706.
(13) Lines, A. M.; Nelson, G. L.; Casella, A. J.; Bello, J. M.; Clark, S. B.; Bryan, S. A. Multivariate Analysis To Quantify Species in the Presence of Direct Interferents: Micro-Raman Analysis of

HNO_3 in Microfluidic Devices. *Anal Chem* **2018**, *90* (4), 2548-2554. DOI: 10.1021/acs.analchem.7b03833.
(14) Lines, A. M.; Tse, P.; Felmy, H. M.; Wilson, J. M.; Shafer, J.; Denslow, K. M.; Still, A. N.; King, C.; Bryan, S. A. Online, Real-Time Analysis of Highly Complex Processing Streams: Quantification of Analytes in Hanford Tank Sample. *Industrial & Engineering Chemistry Research* **2019**, *58* (47), 21194-21200. DOI: 10.1021/acs.iecr.9b03636.
(15) Tse, P.; Bryan, S. A.; Bessen, N. P.; Lines, A. M.; Shafer, J. C. Review of on-line and near real-time spectroscopic monitoring of processes relevant to nuclear material management. *Anal Chim Acta* **2020**, *1107*, 1-13. DOI: 10.1016/j.aca.2020.02.008 From NLM PubMed-not-MEDLINE.
(16) Branch, S. D.; Felmy, H. M.; Schafer Medina, A.; Bryan, S. A.; Lines, A. M. Exploring the Complex Chemistry of Uranium within Molten Chloride Salts. *Industrial & Engineering Chemistry Research* **2023**, *62* (37), 14901-14909. DOI: 10.1021/acs.iecr.3c02005.
(17) Paviet, P.; Hartmann, T.; Lines, A. M.; Bryan, S. A.; Felmy, H. M.; Glezakou, V.-A.; Nguyen, M.-T.; Medina, A.; Branch, S. D. *Corrosion of Molten Salt Containment Alloys - Fundamental Mechanisms for Corrosion Control and Monitoring*; Pacific Northwest National Laboratory, Richland, Washington, 2020.
(18) Lines, A. M.; Bryan, S. A.; Felmy, H. M.; branch, S. D. On-line Monitoring for Molten Salt Reactor MC&A: Optical Spectroscopy-Based Approaches, PNNL-33367. Pacific Northwest National Laboratory Richland, WA, 2022.
(19) Cipiti, B. B.; Warner, D.; Le Blanc, K.; Evans, A.; Russell, J. R.; Shoman, N.; Taconi, A.; Rowland, M.; Lamb, C.; Maccarone, L.; et al. Advanced Reactor Safeguards & Security 2024 Program Roadmap, SAND2024-09669R. Sandia National Laboratories United States, 2024.
(20) Kurley, J. M.; Halstenberg, P. W.; McAlister, A.; Raiman, S.; Dai, S.; Mayes, R. T. Enabling chloride salts for thermal energy storage: implications of salt purity. *RSC Advances* **2019**, *9* (44), 25602-25608, 10.1039/C9RA03133B. DOI: 10.1039/C9RA03133B.
(21) Zhao, Y. *Molten Chloride Thermophysical Properties, Chemical Optimization, and Purification*; United States, 2020. https://www.osti.gov/biblio/1734652 https://www.osti.gov/servlets/purl/1734652DOI: 10.2172/1734652.
(22) Choi, S.; Steppan, J.; Simpson, M. F. Long-Term Stability of Mullite and Magnesia-encased Ag|Ag^+ Reference Electrodes in Molten $MgCl_2$-KCl-NaCl. *Journal of The Electrochemical Society* **2023**, *170* (5), 057505. DOI: 10.1149/1945-7111/acd35a.
(23) Morss, L. R.; Fujino, T. Preparation and crystal structures of plutonium(IV) hexachloro complexes, Rb_2PuCl_6 and K_2PuCl_6. *Journal of Solid State Chemistry* **1988**, *72* (2), 338-352. DOI: https://doi.org/10.1016/0022-4596(88)90038-2.
(24) Branch, S. D.; Felmy, H. M.; Rakos, J. M.; Choi, S.; Heller, F. D.; Bryan, S. A.; Lines, A. M. Optical techniques for advanced salt systems, PNNL-36705. Laboratory, P. N. N., Ed.; Richland, WA, 2024.
(25) Branch, S. D.; Felmy, H. M.; Bryan, S. A.; Lines, A. M. Testing Application of Optical Techniques to Advanced Salt Systems, PNNL-34804. Pacific Northwest National, L., Ed.; Richland, WA, 2023.
(26) Martinot, L.; Fuger, J. Determination of solubility products of various actinide oxides in the (Na-K)Cl AND (Li-K)Cl eutectics and calculation of new potential-pO^{2-} diagrams. *Journal of the Less Common Metals* **1986**, *120* (2), 255-266. DOI: https://doi.org/10.1016/0022-5088(86)90650-8.
(27) Kitawaki, S.; Nakayoshi, A.; Fukushima, M.; Yahagi, N.; Kurata, M. Chemical Form of Actinide Elements Contained in Anode Residue Generated in Electrolysis and the Conversion to Chlorides Using $ZrCl_4$. *Nuclear Technology* **2010**, *171* (3), 285-291. DOI: 10.13182/NT10-A10863.
(28) Williams, D. F. Assessment of candidate molten salt coolants for the NGNP/NHI heat-transfer loop, ORNL/TM-2006/69. Laboratory, O. R. N., Ed.; Oak Ridge, TN, 2006.

(29) Barbanel, Y. A.; Kolin, V. V.; Kotlin, V. P.; Lumpov, A. A. Coordination chemistry of actinides in molten salts. *Journal of Radioanalytical and Nuclear Chemistry Articles* **1990**, *143* (1), 167-179. DOI: 10.1007/BF02117559.
(30) Swanson, J. L. Plutonyl Species in Molten Chloride Salt Solutions. *The Journal of Physical Chemistry* **1964**, *68* (2), 438-439. DOI: 10.1021/j100784a519.
(31) Lambert, H. Molten salt spectroscopy and electrochemistry for spent nuclear fuel treatment. The University of Manchester (United Kingdom), 2017.
(32) Bamberger, C. E.; Ross, R. G.; Baes, C. F.; Young, J. P. Absence of an effect of oxide on the solubility and the absorption spectra of PuF_3 in molten LiF-BeF_2-ThF_4 and the instability of plutonium(III) oxyfluorides. *Journal of Inorganic and Nuclear Chemistry* **1971**, *33* (10), 3591-3594. DOI: 10.1016/0022-1902(71)80687-5.
(33) Kim, B. Y.; Yun, J.-I. Optical absorption and fluorescence properties of trivalent lanthanide chlorides in high temperature molten LiCl–KCl eutectic. *Journal of Luminescence* **2016**, *178*, 331-339. DOI: https://doi.org/10.1016/j.jlumin.2016.06.010.
(34) Felmy, H. M.; Bessen, N. P.; Lackey, H. E.; Bryan, S. A.; Lines, A. M. Quantification of Uranium in Complex Acid Media: Understanding Speciation and Mitigating for Band Shifts. *ACS Omega* **2023**, *8* (44), 41696-41707. DOI: 10.1021/acsomega.3c06007.
(35) Madic, C.; Begun, G. M.; Hobart, D. E.; Hahn, R. L. Raman spectroscopy of neptunyl and plutonyl ions in aqueous solution: hydrolysis of neptunium(VI) and plutonium(VI) and disproportionation of plutonium(V). *Inorganic Chemistry* **1984**, *23* (13), 1914-1921. DOI: 10.1021/ic00181a025.